

Analytical Model of a Dual Rotor Radial Flux Wind Generator Using Ferrite Magnets

Authors:

Peifeng Xu, Kai Shi, Yuxin Sun, Huangqiu Zhu

Date Submitted: 2019-01-31

Keywords: Optimization, ferrite magnets, finite element method, analytical model, equivalent magnetic circuit, dual rotor radial flux wind generator

Abstract:

This paper presents a comprehensive analytical model for dual rotor radial flux wind generators based on the equivalent magnetic circuit method. This model is developed to predict the flux densities of the inner and outer air gaps, flux densities of the rotor and stator yokes, back electromotive force (EMF), electromagnetic torque, cogging torque, and some other characteristics important for generator design. The 2D finite element method (FEM) is employed to verify the presented analytical model, fine-tune it, and validate the prediction precision. The results show that the errors between the proposed analytical model and the FEM results are less than 5% and even less than 1% for certain parameters, that is, the results obtained from the proposed analytical model match well the ones obtained from FEM analysis. Meanwhile, the working points at different temperatures are confirmed to exceed the knee point of the BH curve, which means that irreversible demagnetization does not occur. Finally, the optimization by FEM with the objective of fully using the inner space of the generator, decreasing the cogging torque, and reducing the total harmonic distortion (THD) of back EMF is performed.

Record Type: Published Article

Submitted To: LAPSE (Living Archive for Process Systems Engineering)

Citation (overall record, always the latest version):

LAPSE:2019.0164

Citation (this specific file, latest version):

LAPSE:2019.0164-1

Citation (this specific file, this version):

LAPSE:2019.0164-1v1

DOI of Published Version: <https://doi.org/10.3390/en9090672>

License: Creative Commons Attribution 4.0 International (CC BY 4.0)

Article

Analytical Model of a Dual Rotor Radial Flux Wind Generator Using Ferrite Magnets

Peifeng Xu, Kai Shi *, Yuxin Sun and Huangqiu Zhu

School of Electrical and Information Engineering, Jiangsu University, Zhenjiang 212013, China; xupeifeng2003@126.com (P.X.); syx4461@ujs.edu.cn (Y.S.); zhuhuangqiu@ujs.edu.cn (H.Z.)

* Correspondence: shikai80614@163.com; Tel.: +86-511-8879-1245

Academic Editor: Frede Blaabjerg

Received: 9 July 2016; Accepted: 18 August 2016; Published: 24 August 2016

Abstract: This paper presents a comprehensive analytical model for dual rotor radial flux wind generators based on the equivalent magnetic circuit method. This model is developed to predict the flux densities of the inner and outer air gaps, flux densities of the rotor and stator yokes, back electromotive force (EMF), electromagnetic torque, cogging torque, and some other characteristics important for generator design. The 2D finite element method (FEM) is employed to verify the presented analytical model, fine-tune it, and validate the prediction precision. The results show that the errors between the proposed analytical model and the FEM results are less than 5% and even less than 1% for certain parameters, that is, the results obtained from the proposed analytical model match well the ones obtained from FEM analysis. Meanwhile, the working points at different temperatures are confirmed to exceed the knee point of the BH curve, which means that irreversible demagnetization does not occur. Finally, the optimization by FEM with the objective of fully using the inner space of the generator, decreasing the cogging torque, and reducing the total harmonic distortion (THD) of back EMF is performed.

Keywords: dual rotor radial flux wind generator; analytical model; equivalent magnetic circuit; ferrite magnets; finite element method; optimization

1. Introduction

Wind power generation, as the most competitive and clean renewable energy technology, is attracting more and more attention all over the world. In wind energy conversion systems, permanent magnet generators (PMGs) have been widely used for their numerous advantages such as simple structure, high efficiency, reliable operation and no need for an additional power supply due to the magnet field excitation. Most PMGs contain rare-earth permanent magnet materials, namely, NdFeB grades, for their high remanence and coercivity values [1–5]. However, the cost of NdFeB magnets has increased significantly over the last several years and there is an increasing concern about the stable supply of the raw material for NdFeB [6]. With this consideration, generators with less or without rare-earth materials are required in wind power applications to reduce the machinery cost [7].

Ferrite magnet material has many merits, such as low weight density, low cost, and stainless nature, etc. PMGs using ferrite magnets were studied in [8–10]. Due to the relatively low residual flux density of ferrite magnet material, it is obvious that the performance is dramatically decreased when a ferrite magnet with 0.4 T of remanence is used instead of a NdFeB magnet [11]. In order to resolve this problem, the dual rotor permanent magnet (PM) machine using ferrite magnets was proposed [12]. When using NdFeB magnets, the dual rotor permanent magnet (DRPM) machine can significantly improve the torque density and efficiency owing to the special structure of double rotors and dual air-gaps. In fact, the improvement of torque density is achieved by doubling the working portion of the air gap [13,14]. Accordingly, the torque density and efficiency of the DRPM wind generator using

ferrite magnets are higher than those of traditional PM generators using ferrite magnets. Qu designed a dual rotor permanent magnet (DRPM) motor using ferrite magnets in [15]. In [16] he came to the conclusion that the torque density of a DRPM is almost three times the density of a commercial induction motor (IM) and 2.2 times the density of a commercial interior PM (IPM) machine with an efficiency just slightly lower than that of an IPM machine, but higher than that of an IM. Hence, we may consider transplanting the dual rotor machine using ferrite to wind power generation.

DRPM machines include dual rotor radial flux PM machines and dual rotor axial flux PM machines [17]. In general, dual rotor radial flux (DRRF) and dual rotor axial flux (DRAF) machines have similar torque density, torque-to-mass ratio, losses, and efficiency performance. However, the material cost of DRAF machines is much higher than that of DRRF machines due to more magnets being required for DRAF machines. Meanwhile, the DRRF machines need and can provide stronger cooling capability than DRAF machines [18]. As a consequence, this paper proposes a DRRF wind generator using ferrite magnets.

When performing preliminary design of an electric machine, the equivalent magnetic circuit (EMC) approach is a popular choice for designers due to its fast and analytical nature [19]. EMC needs empirical coefficients to correct the magnetic saturation and leakage flux conditions. Those coefficients are easily affected by many factors, including the operation state and magnetic saturation level, so the precision of the EMC approach is not high enough to use in practice. The finite element method (FEM), as a numerical method, is a numerically accurate algorithm [20], but is too time-consuming. Considering the fast performance of EMC and high accuracy of FEM, the analytical approach combining EMC and FEM should be a good compromise between simplicity and accuracy. This approach is useful and effective in the preliminary design of an electrical machine.

The main contribution of this paper is the development of a comprehensive analytical model for a DRRF wind generator based on EMC. The elements of this analytical model are precisely calculated in cylindrical coordinates to achieve a high accuracy. The proposed model takes into account the iron saturation, all generator dimensions as well as material properties, and is able to accurately predict the electromotive force (EMF), torque and cogging torque, as well as numerous other design aspects. The results of the proposed model are then evaluated and verified by FEM. The errors between the proposed model and FEM model are less than 5% for flux densities, 3% for EMF, and even as low as 1% for electromagnetic torque, which are basic parameters used to verify the feasibility of the proposed model. In addition, the working points at different temperatures are measured to determine whether the ferrite magnets are demagnetized or not, and the corresponding results indicate that irreversible demagnetization does not occur.

At the end of this paper, the optimization to achieve specific design objectives, such as making the best use of the inner space of the DRRF generator, decreasing the cogging torque, and reducing the total harmonic distribution (THD) of the back EMF, is presented. Consequently, the optimal split ratio of the inner and outer stator radius, the pole arc ratio of the inner and outer rotors, and the outer slot opening are determined.

2. Modeling

2.1. Machine Topology

Figure 1 illustrates the configuration and linear topology of the DRRF wind generator. Therein, a cup stator is sandwiched between two concentric rotors. The radially polarized surface mounted ferrite magnets are placed on the air-gap sides of the inner and outer rotors. For the sake of a smaller effective air gap, the stator is slotted on both sides to enhance the power density. The back-to-back toroidally wound winding is adopted, which brings advantages such as short end winding length, less copper loss, and simple maintenance. In some sense, the DRRF generator can be seen as one inner rotor generator nested inside one outer rotor generator.

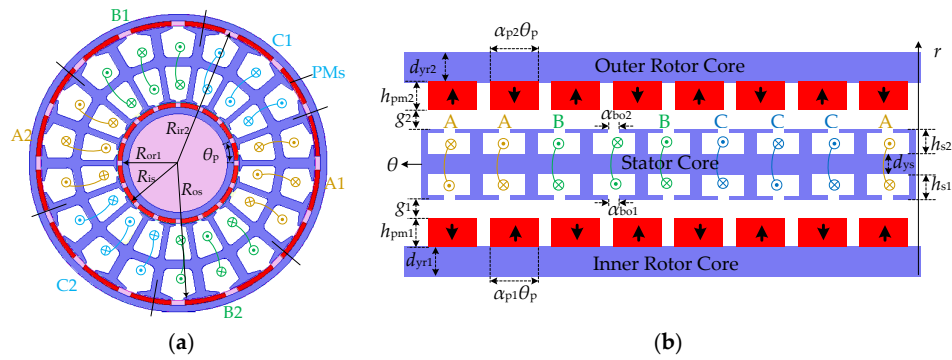


Figure 1. Configuration and linear topology of the proposed dual rotor radial flux (DRRF) wind generator: (a) Configuration; (b) Linear topology.

The variables defined in Figure 1 are:

| | |
|------------------|---|
| R_{or1} | outer radius of the inner rotor |
| R_{ir2} | inner radius of the outer rotor |
| R_{is} | inner radius of the stator |
| R_{os} | outer radius of the stator |
| θ_p | pole pitch angle |
| m | number of phase |
| p | machine pole pairs |
| N_s | inner or outer slot number |
| $\alpha_{p1,2}$ | pole arc ratio of the inner/outer rotor |
| L | effective stack length |
| $h_{pm1,2}$ | thickness of the inner/outer magnets |
| $\alpha_{bo1,2}$ | the inner/outer slot opening angle |
| $h_{s1,2}$ | height of the inner/outer slots |
| $g_{1,2}$ | length of the inner/outer air gap |
| $d_{yr1,2}$ | thickness of the inner/outer rotor yoke |

2.2. Analytical Model

The linear translational topology and the corresponding EMC of the DRRF wind generator are presented and shown in Figure 2a,b, respectively, where the leakage flux, iron saturation as well as machine dimensions are taken into account.

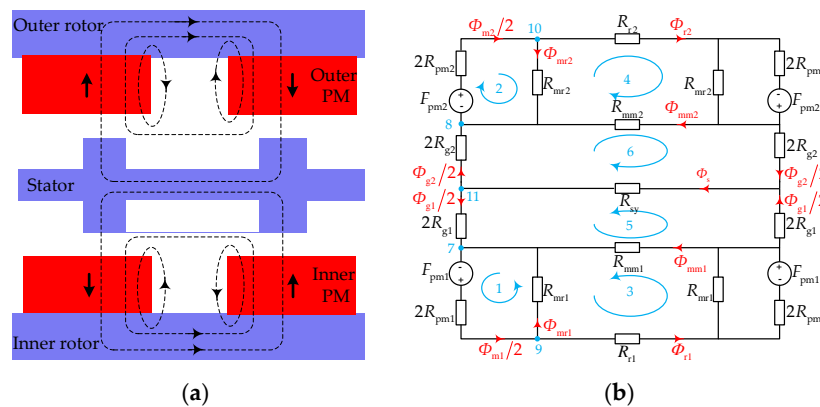


Figure 2. The linear translational topology and the corresponding equivalent magnetic circuit (EMC) of the DRRF wind generator: (a) The linear translational topology; (b) The corresponding EMC.

In this EMC, Φ_{m1} and Φ_{m2} are the fluxes leaving the inner and outer magnets respectively, Φ_{mr1} and Φ_{mr2} are the inner and outer leakage fluxes between the magnet and rotor yoke, Φ_{r1} and Φ_{r2} are the fluxes going through the inner and outer rotor yokes, Φ_{mm1} and Φ_{mm2} are the leakage fluxes between the adjacent inner and outer magnets, Φ_{g1} and Φ_{g2} are the fluxes passing through the inner and outer air gaps, and Φ_s is the flux passing through the stator yoke. The equivalent magneto motive forces (MMFs) of the inner and outer magnets are respectively given by:

$$F_{pm1} = h_{pm1} |H_c|; F_{pm2} = h_{pm2} |H_c| \quad (1)$$

where H_c is the coercivity of the ferrite magnets.

The reluctance of the inner magnet can be calculated from [21]:

$$R_{pm1} = \frac{1}{\mu_0 \mu_r} \int_{R_{or1}}^{R_{or1} + h_{pm1}} \frac{dr}{r \alpha_{p1} \theta_p L} = \frac{1}{\mu_0 \mu_r \alpha_{p1} \theta_p L} \ln \left[1 + \frac{h_{pm1}}{R_{or1}} \right] \quad (2)$$

Similar to the inner magnet, the reluctance of the outer magnet is:

$$R_{pm2} = \frac{1}{\mu_0 \mu_r \alpha_{p2} \theta_p L} \ln \left[1 + \frac{h_{pm2}}{R_{ir2} - h_{pm2}} \right] \quad (3)$$

where μ_r is the relatively recoil permeability of the ferrite magnets.

The half circle shaped model is one of the most precise techniques for modeling flux flowing in the inner and outer air gaps as depicted in Figure 3a,b. At each side of the inner and outer air gaps, the length of the fringing fluxes $L_i(r)$ and $L_o(r)$ can be calculated by:

$$L_i(r) = \sqrt{(g_{e1}/2)^2 - |r - R_{or1} - h_{pm1} - g_{e1}/2|^2} \quad (4)$$

$$L_o(r) = \sqrt{(g_{e2}/2)^2 - |R_{ir2} - h_{pm2} - g_{e2}/2 - r|^2} \quad (5)$$

$$g_{e1} = K_{c1} g_1; g_{e2} = K_{c2} g_2 \quad (6)$$

where g_{e1} and g_{e2} are the effective lengths of the inner and outer air gaps taking into account the stator slotting, K_{c1} and K_{c2} are the inner and outer Carter's coefficients respectively [21]:

$$K_{c1} = \frac{\tau_{s1}}{\tau_{s1} - \frac{2\alpha_{bo1}R_{is}}{\pi} \left\{ \tan^{-1} \frac{\alpha_{bo1}R_{is}}{2g_1} - \frac{g_1}{\alpha_{bo1}R_{is}} \ln \left[1 + \left(\frac{\alpha_{bo1}R_{is}}{2g_1} \right)^2 \right] \right\}} \quad (7)$$

$$K_{c2} = \frac{\tau_{s2}}{\tau_{s2} - \frac{2\alpha_{bo2}R_{os}}{\pi} \left\{ \tan^{-1} \frac{\alpha_{bo2}R_{os}}{2g_2} - \frac{g_2}{\alpha_{bo2}R_{os}} \ln \left[1 + \left(\frac{\alpha_{bo2}R_{os}}{2g_2} \right)^2 \right] \right\}} \quad (8)$$

$$\tau_{s1} = \frac{2\pi R_{is}}{N_s}; \tau_{s2} = \frac{2\pi R_{os}}{N_s} \quad (9)$$

where τ_{s1} and τ_{s2} are the inner and outer slot pitches.

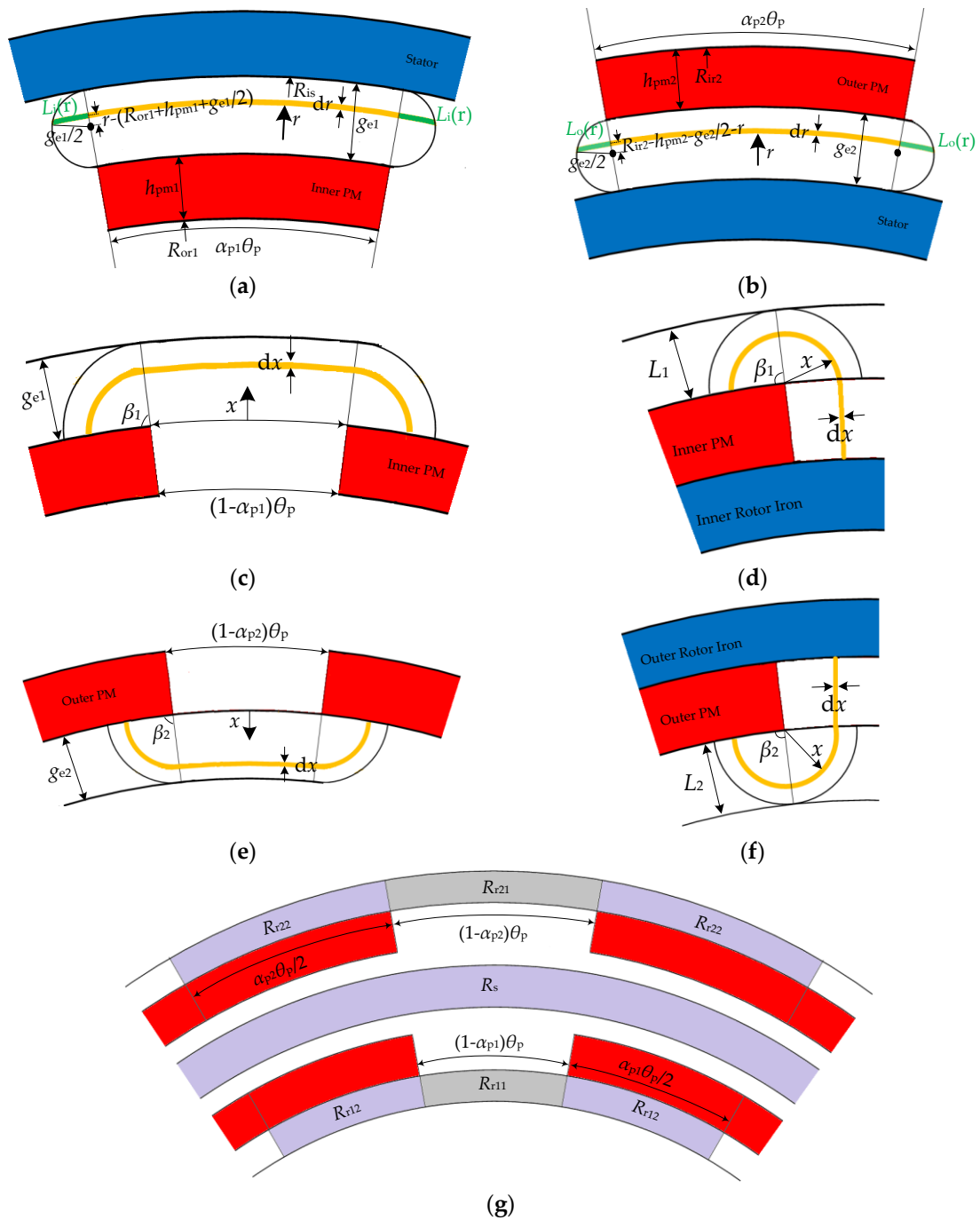


Figure 3. The flux path for calculating: (a) The effective inner air gap reluctance; (b) The effective outer air gap reluctance; (c) The inner magnet to magnet leakage reluctance; (d) The inner magnet to inner rotor iron leakage reluctance; (e) The outer magnet to magnet leakage permeance; (f) The outer magnet to iron leakage reluctance; (g) The rotor yokes reluctances.

The effective reluctances of the inner and outer air gaps can be calculated by the trapezoidal integral as:

$$R_{g1} = \frac{1}{\mu_0 L} \int_{R_{or1}+h_{pm1}}^{R_{or1}+h_{pm1}+g_{e1}} \frac{dr}{r\alpha_{p1}\theta_p + 2L_i(r)} \quad (10)$$

$$R_{g2} = \frac{1}{\mu_0 L} \int_{R_{ir2}-h_{pm2}-g_{e2}}^{R_{ir2}-h_{pm2}} \frac{dr}{r\alpha_{p2}\theta_p + 2L_o(r)} \quad (11)$$

The arc shaped model of the leakage permeance between two adjacent inner magnets is shown in Figure 3c. And the leakage permeance of the inner magnets will be:

$$\Lambda_{mm1} = \frac{1}{R_{mm1}} = \mu_0 L \int_0^{g_{e1}} \frac{dx}{2\beta_1 x + (R_{or1} + h_{pm1} + x)(1 - \alpha_{p1})\theta_p} \quad (12)$$

$$\beta_1 = \pi - \arccos \frac{g_{e1}/2}{R_{or1} + h_{pm1}} \quad (13)$$

So Λ_{mm1} can be further expressed as:

$$\Lambda_{mm1} = \frac{\mu_0 L}{2\beta_1 + (1 - \alpha_{p1})\theta_p} \ln \left[1 + \frac{2\beta_1 g_{e1} + (1 - \alpha_{p1})\theta_p}{(R_{or1} + h_{pm1})(1 - \alpha_{p1})\theta_p} \right] \quad (14)$$

According to the model shown in Figure 3d, the leakage permeance between the inner magnet and inner rotor iron can be calculated from:

$$\Lambda_{mr1} = \frac{1}{R_{mr1}} = \mu_0 L \int_0^{L_1} \frac{dx}{2\beta_1 x + h_{pm1}} \quad (15)$$

$$L_1(\alpha_{p1}) = \min [g_{e1}, (R_{or1} + h_{pm1})(1 - \alpha_{p1})\theta_p / 2] \quad (16)$$

and then Λ_{mr1} can be further expressed as:

$$\Lambda_{mr1} = \frac{\mu_0 L}{2\beta_1} \ln \left[1 + \frac{2\beta_1 L_1}{h_{pm1}} \right] \quad (17)$$

For two adjacent outer magnets, according to Figure 3e:

$$\beta_2 = \arccos \frac{g_{e2}/2}{R_{ir2} - h_{pm2}} \quad (18)$$

so the leakage permeance of the outer magnets is:

$$\begin{aligned} \Lambda_{mm2} &= \frac{1}{R_{mm2}} = \mu_0 L \int_0^{g_{e2}} \frac{dx}{2\beta_2 x + (R_{ir2} - h_{pm2} - x)(1 - \alpha_{p2})\theta_p} \\ &= \frac{\mu_0 L}{2\beta_2 - (1 - \alpha_{p2})\theta_p} \ln \left[1 + \frac{g_{e2}[2\beta_2 - (1 - \alpha_{p2})\theta_p]}{(R_{ir2} - h_{pm2})(1 - \alpha_{p2})\theta_p} \right] \end{aligned} \quad (19)$$

Similarly, according to Figure 3f the leakage permeance between the outer magnet and outer rotor iron can be calculated by:

$$\Lambda_{mr2} = \frac{1}{R_{mr2}} = \mu_0 L \int_0^{L_2} \frac{dx}{2\beta_2 x + h_{pm2}} \quad (20)$$

$$L_2(\alpha_{p2}) = \min [g_{e2}, (R_{ir2} - h_{pm2})(1 - \alpha_{p2})\theta_p / 2] \quad (21)$$

and Λ_{mr2} can be further expressed as:

$$\Lambda_{mr2} = \frac{\mu_0 L}{2\beta_2} \ln \left[1 + \frac{2\beta_2 L_2}{h_{pm2}} \right] \quad (22)$$

As shown in Figure 3g, the total reluctances of the inner and outer rotors are:

$$R_{r1} = R_{r11} + 2R_{r12}; \quad R_{r2} = R_{r21} + 2R_{r22} \quad (23)$$

Reluctances adjacent to the inter-polar regions are:

$$R_{r11} = \frac{(R_{or1} - d_{yr1}/2)(1 - \alpha_{p1})\theta_p}{\mu_0 \mu_{r1} A_{11}} \quad (24)$$

$$R_{r21} = \frac{(R_{ir2} + d_{yr2}/2)(1 - \alpha_{p2})\theta_p}{\mu_0 \mu_{r1} A_{21}} \quad (25)$$

$$A_{11} = d_{yr1}L; A_{21} = d_{yr2}L \quad (26)$$

where A_{11} and A_{21} are the areas passing through the corresponding yoke flux flow. Making use of the average area of the surfaces, reluctances adjacent to the magnets are:

$$R_{r12} = \frac{0.5\alpha_{p1}\theta_p(R_{or1} - d_{yr1}/2)}{\mu_0 \mu_{r2}(A_{11} + A_{12})/2} \quad (27)$$

$$R_{r22} = \frac{0.5\alpha_{p2}\theta_p(R_{ir2} + d_{yr2}/2)}{\mu_0 \mu_{r2}(A_{21} + A_{22})/2} \quad (28)$$

$$A_{12} = 0.5\alpha_{p1}\theta_p R_{or1}L; A_{22} = 0.5\alpha_{p2}\theta_p R_{ir2}L \quad (29)$$

where μ_{r1} , μ_{r2} are the relatively permeabilities of the corresponding iron parts. They change with the flux densities inside the iron parts.

The reluctance of the stator yoke is:

$$R_{sy} = \frac{N_s}{2p} \frac{(R_{is} + kR_{os})/(k+1)}{\mu_0 \mu_{r1} d_{ys}L}; k = \frac{h_{s1}}{h_{s2}} \quad (30)$$

Applying the Kirchhoff's circuit law (KCL) and Kirchhoff's voltage law (KVL) to the loops and nodes in Figure 2, some relationships can be obtained:

$$R_{pm1}\Phi_{m1} + R_{mr1}\Phi_{mr1} = F_{pm1}; R_{pm2}\Phi_{m2} + R_{mr2}\Phi_{mr2} = F_{pm2} \quad (31)$$

$$R_{mm1}\Phi_{mm1} - 2R_{mr1}\Phi_{mr1} + R_{r1}\Phi_{r1} = 0; R_{mm2}\Phi_{mm2} - 2R_{mr2}\Phi_{mr2} + R_{r2}\Phi_{r2} = 0 \quad (32)$$

$$2R_{g1}\Phi_{g1} - R_{mm1}\Phi_{mm1} + R_s\Phi_s = 0; 2R_{g2}\Phi_{g2} - R_{mm2}\Phi_{mm2} + R_s\Phi_s = 0 \quad (33)$$

$$0.5\Phi_{g1} + \Phi_{mm1} + \Phi_{mr1} = 0.5\Phi_{m1}; 0.5\Phi_{g2} + \Phi_{mm2} + \Phi_{mr2} = 0.5\Phi_{m2} \quad (34)$$

$$\Phi_{mr1} + \Phi_{r1} = 0.5\Phi_{m1}; \Phi_{mr2} + \Phi_{r2} = 0.5\Phi_{m2} \quad (35)$$

$$0.5\Phi_{g1} + 0.5\Phi_{g2} = \Phi_s \quad (36)$$

By calculating these equations, all fluxes flowing into the circuit elements can be obtained. As a result, the flux densities corresponding to reluctances R_{r11} , R_{r12} , R_{r21} , R_{r22} and R_{sy} can be calculated by:

$$B_{r11} = \frac{\Phi_{r1}}{A_{11}}; B_{r12} = \frac{\Phi_{r1}}{(A_{11} + A_{12})/2} \quad (37)$$

$$B_{r21} = \frac{\Phi_{r2}}{A_{21}}; B_{r22} = \frac{\Phi_{r2}}{(A_{21} + A_{22})/2} \quad (38)$$

$$B_s = \frac{\Phi_s}{d_{ys}L} \quad (39)$$

According to (37) and (38), a conclusion can be drawn that the flux densities adjacent to the inter-polar regions are higher than those adjacent to the magnets, and the flux densities within the inner and outer air gaps are respectively:

$$B_{g1} = \frac{\Phi_{g1}}{[r\alpha_{p1}\theta_p + 2L_i(r)]L}; B_{g2} = \frac{\Phi_{g2}}{[r\alpha_{p2}\theta_p + 2L_o(r)]L} \quad (40)$$

2.3. Back Electromotive Force (EMF) Derivation

Before the EMF can be found, it is necessary to obtain the fundamental components B_{1g1} and B_{1g2} of the flux densities in the inner and outer air gaps. When the leakage flux is neglected, all the air gap flux flows into the air gap through the magnet surface. In this situation, the air gap flux density is an approximate square wave as shown in Figure 4 in green, and its fundamental component obtained by Fast Fourier Transform (FFT) is shown in Figure 4b in red, where α_p is the pole arc ratio of the rotor.

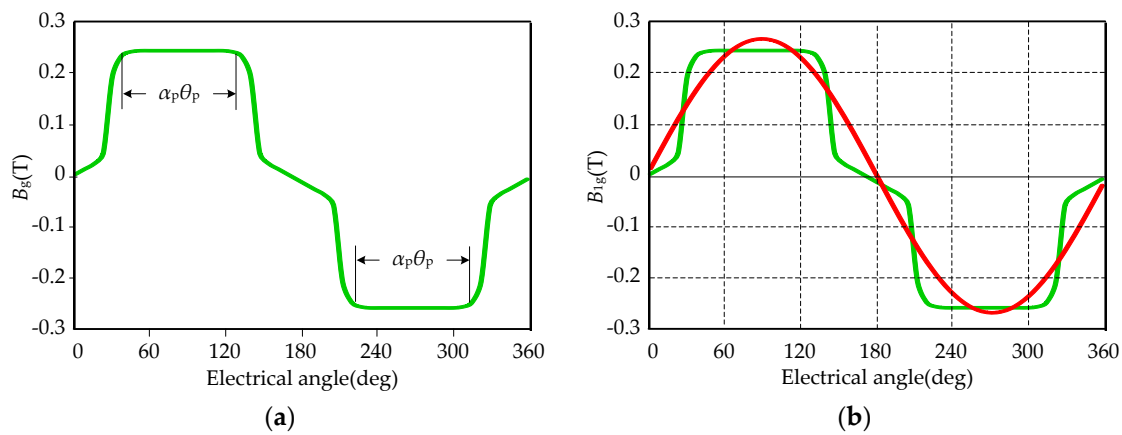


Figure 4. The air gap flux density waveform under a pair of poles of conventional surface mounted pole structure and its fundamental component: (a) The air gap flux density; (b) The fundamental component of the air gap flux density.

Based on FFT, the fundamental components of the inner and outer air gap flux densities, B_{1g1} and B_{1g2} can be calculated by:

$$B_{1g1} = \frac{2\sqrt{2}}{\pi} \alpha_{p1} \sin\left(\frac{1}{2} \alpha_{p1} \theta_p\right) B_{g1}; B_{1g2} = \frac{2\sqrt{2}}{\pi} \alpha_{p2} \sin\left(\frac{1}{2} \alpha_{p2} \theta_p\right) B_{g2} \quad (41)$$

For an alternating current (AC) machine, it is well known that the induced root mean square (RMS) voltage per phase of a concentrated winding is given by:

$$E_f = 4.44 f N_{ph} \Phi_f \quad (42)$$

where the subscript “f” denotes the fundamental, f is the frequency, N_{ph} is the total number of turns in series per phase, and Φ_f is the fundamental flux per pole.

For the sake of dual air gap structure, the phase EMF of the DRRF wind generator is the sum of the EMF induced by the flux linkage in both inner and outer air gaps. Given $N_{ph}/2$ turns for both inner and outer slots, the induced RMS phase voltage is:

$$E_f = E_{f1} + E_{f2} = 4.44 f \frac{N_{ph}}{2} (\Phi_{f1} + \Phi_{f2}) \quad (43)$$

$$\Phi_{f1} = \frac{2}{\pi} \sqrt{2} B_{1g1} \tau_{p1} L; \Phi_{f2} = \frac{2}{\pi} \sqrt{2} B_{1g2} \tau_{p2} L \quad (44)$$

where τ_{p1} , τ_{p2} are the inner and outer pole pitches, respectively:

$$\tau_{p1} = \frac{2\pi R_{is}}{2p} = \frac{\pi R_{is}}{p}; \tau_{p2} = \frac{\pi R_{os}}{p} \quad (45)$$

When the fundamental distribution factor, the pitch factor, the skew factor for the distributed fractional-pitch, and skewed magnets are applied, the voltage is modified to:

$$E_f = 4.44\sqrt{2}K_w f N_{ph} (B_{1g1} R_{is} + B_{1g2} R_{os}) L / p \quad (46)$$

where K_w is the winding factor for the fundamental.

2.4. Voltage Equation and Torque Derivation

When neglecting the slot opening height, the average coil length per turn is given by:

$$L_c = 2L + 2d_{ys} + 2h_{s1} + 2h_{s2} + g_1 + g_2 \quad (47)$$

The phase resistance R_s is:

$$R_s = \frac{\rho L_c N_{ph}}{C A_w} \quad (48)$$

$$A_w = \frac{A_{slot} K_{cu}}{N_c}; N_c = \frac{m C N_{ph}}{N_s} \quad (49)$$

where ρ is the winding material resistivity, C is the number of parallel circuits of the winding, A_w is the available bare wire area, K_{cu} is stator bare copper filling factor, and N_c is the number of conductors in each slot. For the DRRF generator, due to the adoption of back-to-back toroidally wound winding, the area of the inner slot should equal to that of the outer one A_{slot} in order to take full advantage of the inner space.

The voltage of the DRRF wind generator in synchronously rotating dq reference frame can be expressed by:

$$u_d = R_s i_d + \frac{d\psi_{sd}}{dt} - \omega \psi_{sq}; u_q = R_s i_q + \frac{d\psi_{sq}}{dt} + \omega \psi_{sd} \quad (50)$$

where u_d and u_q are the d and q axis stator voltages, i_d and i_q are the d and q axis stator currents, ψ_{sd} and ψ_{sq} are the d and q axis flux linkages of the stator, and ω is the angular electrical speed.

The flux linkage equations can be expressed as:

$$\psi_{sd} = L_d i_d + \psi_m; \psi_{sq} = L_q i_q \quad (51)$$

where L_d and L_q are the d and q axis inductances, and ψ_m is the permanent magnet flux linkage.

The electromagnetic torque can be expressed as:

$$T_{em} = \frac{3}{2} p (\psi_{sd} i_q - \psi_{sq} i_d) = \frac{3}{2} p (\psi_m i_q - (L_d - L_q) i_d i_q) \quad (52)$$

From (52), it can be seen that the electromagnetic torque consists of two parts: the first part is the torque produced by the magnets, and the second part is the reluctance torque generated due to the saliency effect.

2.5. Cogging Torque Derivation

Cogging torque is caused by the interaction of the rotor magnetic flux and angular variations in stator magnetic reluctance. In detail, cogging torque is produced by the magnetic energy of the field

due to the magnets with the mechanical angular position of the rotor. For the DRRF generator, the cogging torques of the inner and outer rotors are:

$$T_{\text{cog1}} = -\frac{1}{2} \Phi_{g1}^2 \frac{dR_{g1}}{d\theta}; T_{\text{cog2}} = -\frac{1}{2} \Phi_{g2}^2 \frac{dR_{g2}}{d\theta} \quad (53)$$

Equation (53) implies that the cogging torques are caused by the stator slotted on both sides, and that the cogging torques always exist. It should be noted that the air gap reluctances R_{g1} and R_{g2} here are not the average value from Equations (10) and (11). The inner air gap reluctance accounting for the angular position of the rotor relative to the stator teeth will be shown in Figure 5. When the center line of the inner ferrite magnet aligns with the center line of the inner tooth, $\theta = 0$. The air gap corresponding to one half magnet pole can be divided into three parts, P_1 , P_2 , and P_3 .

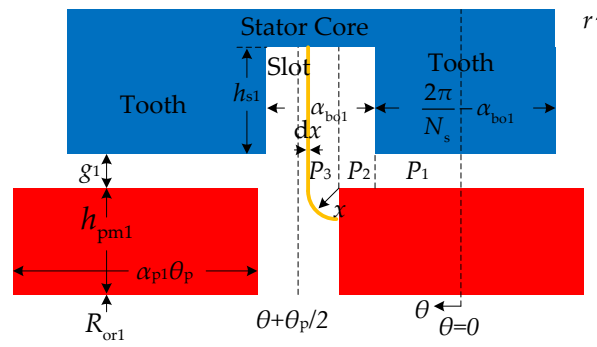


Figure 5. The inner air gap reluctance for cogging torque calculation.

The air gap reluctance of P_1 part can be calculated by:

$$R_1 = \frac{1}{\mu_0 L} \int_{R_{or1}+h_{pm1}}^{R_{or1}+h_{pm1}+g_1} \frac{dr}{\left[\frac{(2\pi/N_s)-\alpha_{bo1}}{2} - \theta \right] r} = \frac{1}{\mu_0 L \left[\frac{(2\pi/N_s)-\alpha_{bo1}}{2} - \theta \right]} \ln \frac{R_{or1}+h_{pm1}+g_1}{R_{or1}+h_{pm1}} \quad (54)$$

The air gap reluctance of P_2 part can be calculated by:

$$\begin{aligned} R_2 &= \frac{1}{\mu_0 L} \int_{R_{or1}+h_{pm1}}^{R_{or1}+h_{pm1}+g_1+h_{s1}} \frac{dr}{\left[\theta + \frac{1}{2} \alpha_{p1} \theta_p - \frac{(2\pi/N_s)-\alpha_{bo1}}{2} \right] r} \\ &= \frac{1}{\mu_0 L \left[\theta + \frac{1}{2} \alpha_{p1} \theta_p - \frac{(2\pi/N_s)-\alpha_{bo1}}{2} \right]} \ln \frac{R_{or1}+h_{pm1}+g_1+h_{s1}}{R_{or1}+h_{pm1}} \end{aligned} \quad (55)$$

The air gap permeance of P_3 part can be calculated by:

$$\Lambda_3 = \int_{\theta+\frac{1}{2}\alpha_{p1}\theta_p}^{\theta+\frac{1}{2}\theta_p} \frac{\mu_0 L dx}{h_{s1}+g_1+\frac{1}{2}\pi x} = \frac{2\mu_0 L}{\pi} \ln \frac{4h_{s1}+4g_1+2\pi\theta+\pi\theta_p}{4h_{s1}+4g_1+2\pi\theta+\pi\alpha_{p1}\theta_p} \quad (56)$$

The air gap reluctance of one half inner magnet pole is:

$$\begin{aligned} R_{g1} &= R_1 + R_2 + \frac{1}{\Lambda_3} = \frac{1}{\mu_0 L \left[\frac{(2\pi/N_s)-\alpha_{bo1}}{2} - \theta \right]} \ln \frac{R_{or1}+h_{pm1}+g_1}{R_{or1}+h_{pm1}} \\ &+ \frac{1}{\mu_0 L \left[\theta + \frac{1}{2} \alpha_{p1} \theta_p - \frac{(2\pi/N_s)-\alpha_{bo1}}{2} \right]} \ln \frac{R_{or1}+h_{pm1}+g_1+h_{s1}}{R_{or1}+h_{pm1}} + \frac{\pi}{2\mu_0 L \ln \frac{4h_{s1}+4g_1+2\pi\theta+\pi\theta_p}{4h_{s1}+4g_1+2\pi\theta+\pi\alpha_{p1}\theta_p}} \end{aligned} \quad (57)$$

Similarly, the air gap reluctance of one half outer magnet pole is:

$$R_{g2} = \frac{1}{\mu_0 L \left[\frac{(2\pi/N_s) - \alpha_{bo2}}{2} - \theta \right]} \ln \frac{R_{ir2} - h_{pm2}}{R_{ir2} - h_{pm2} - g_2} + \frac{1}{\mu_0 L \left[\theta + \frac{1}{2} \alpha_{p2} \theta_p - \frac{(2\pi/N_s) - \alpha_{bo2}}{2} \right]} \ln \frac{R_{ir2} - h_{pm2}}{R_{ir2} - h_{pm2} - g_2 - h_{s2}} + \frac{\pi}{2\mu_0 L \ln \frac{4h_{s2} + 4g_2 + 2\pi\theta + \pi\alpha_p}{4h_{s2} + 4g_2 + 2\pi\theta + \pi\alpha_{p2}\theta_p}} \quad (58)$$

The other part of the inner and outer air gap reluctances can be obtained by symmetry. The cogging torques have a close relation to the tooth harmonic and are affected by the tooth number under a pole pair, and the frequency of cogging torques increases with the slot number. The number of the pulsations of cogging torque in the number of slots can be expressed by:

$$N_{cog} = \frac{2p}{\text{HCD}(N_s, 2p)} \quad (59)$$

where the denominator is the highest common divider (HCD) of the slot number and pole number.

The spatial period of cogging torque T_{sp} can be obtained by the least common multiple (LCM):

$$T_{sp} = \frac{360^\circ}{\text{LCM}(N_s, 2p)} \quad (60)$$

2.6. Design Consideration

During the generator designing process, a number of technical and economic requirements must be taken into account, such as torque, efficiency, material cost, etc. It is often difficult for all these requirements to be satisfied simultaneously. Due to the low remanence, the ferrite magnets are liable to be affected by a demagnetizing field, which results in a serious deterioration of machine performance. Accordingly, it is important to limit the flux density inside the ferrite magnets to avoid the irreversible demagnetization.

3. Model Evaluation

In this section, characteristics of the DRRF wind generator are obtained and evaluated by the proposed analytical model and are compared with those extracted from FEM. The FEM analysis is an auxiliary approach to validate the analytical model, slightly adjust it, and prove its predictions. The primary design specifications and parameters are given in Table 1.

Table 1. Design specifications of the dual rotor radial flux (DRRF) wind generator.

| Specification | Values | Unit |
|--------------------------|--------|------|
| Rated Power | 1.5 | kW |
| Rated Speed | 375 | rpm |
| Rated Voltage | 180 | V |
| Outer Diameter of Stator | 200 | mm |
| Inner Diameter of Stator | 86 | mm |
| Stack Length | 200 | mm |
| Air Gap Length | 0.5 | mm |

Flux line distribution and flux density distribution for both no load and full load conditions are illustrated in Figure 6. It can be found that the flux densities within the portions corresponding to R_{r11} and R_{r21} are higher than those corresponding to R_{r12} and R_{r22} , which verifies the correctness of the analysis result in Figure 3g. By making a comparison between the distributions at no load and full load conditions, it can be seen that some distortions in the flux lines and flux density have appeared for the sake of the armature reaction.

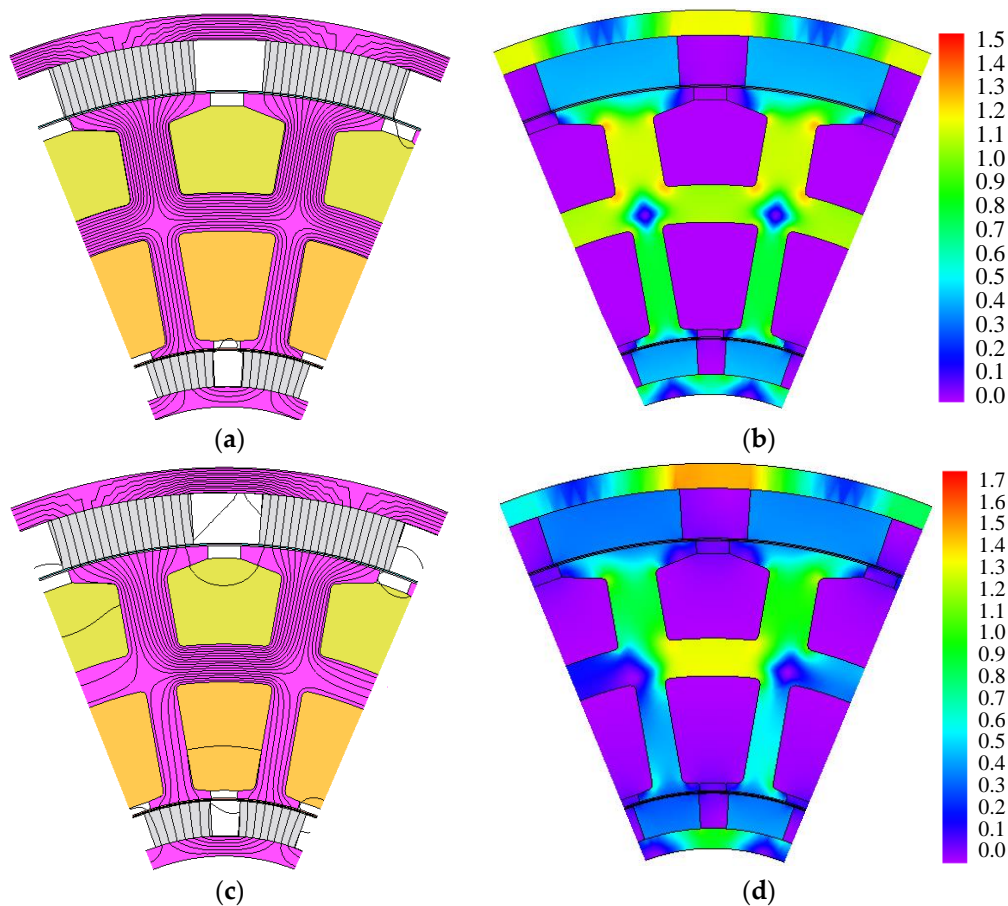


Figure 6. Flux line distribution and flux density distribution at no load and full load: (a) Flux line at no load; (b) Flux density at no load; (c) Flux line at full load; (d) Flux density at full load.

The comparison shown in Table 2 demonstrates that all the designed parameters closely agree to the FEM measurement values, and the errors between them are less than 5%. This implies that the model derived in Section 2 is acceptable as a predictor of machine performance.

Table 2. Comparison of the designed and finite element method (FEM) measured values for the DRRF wind generator.

| Parameter | Designed Value | FEM Value |
|---|----------------|-----------|
| Flux density in inner air gap, B_{g1} (T) | 0.24 | 0.23 |
| Flux density in outer air gap, B_{g2} (T) | 0.273 | 0.265 |
| Flux density in inner rotor core, B_{r11} (T) | 0.4 | 0.39 |
| Flux density in inner rotor core, B_{r12} (T) | 1.02 | 0.97 |
| Flux density in outer rotor core, B_{r21} (T) | 0.376 | 0.36 |
| Flux density in outer rotor core, B_{r22} (T) | 1.28 | 1.22 |
| Flux density in stator core, B_s (T) | 1.52 | 1.45 |

For the no load case, the magnetic fields in the inner and outer air gaps are all generated by ferrite magnets. However, for the load case, the magnetic fields are produced not only by the ferrite magnets but also the armature current. The armature current tends to create a magnetic field with its axis 90° away from the magnetic axis, which is called armature reaction. The effect of armature reaction field is to vary the amplitude and phase of the magnetic field in the air gaps. Figure 7 shows how flux densities in the inner and outer air gaps are altered by the armature current. By comparison, the flux

densities decrease in the one side of magnets while increase in the other side when the generator operates at full load. Due to the low remanence of the ferrite magnet material and the thickness of magnets, the effect of armature reaction is not very severe.

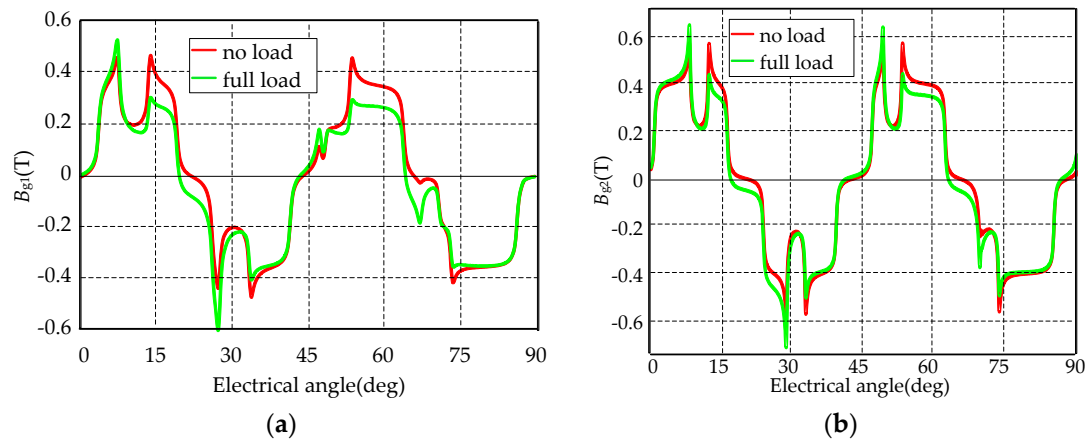


Figure 7. The air gap flux densities at no load and full load: (a) The inner air gap flux densities; (b) The outer air gap flux densities.

The developed back EMF of the proposed DRRF wind generator at the rated speed of 375 rpm is shown in Figure 8. The results are still pretty close to each other, and the maximum discrepancy between them is less than 3%. As shown in Figure 8, the waveform of the EMF is nearly sinusoidal and the THD is about 2.4%. The peak value obtained by the analytical model is about 185 V, which is slightly larger than the design value.

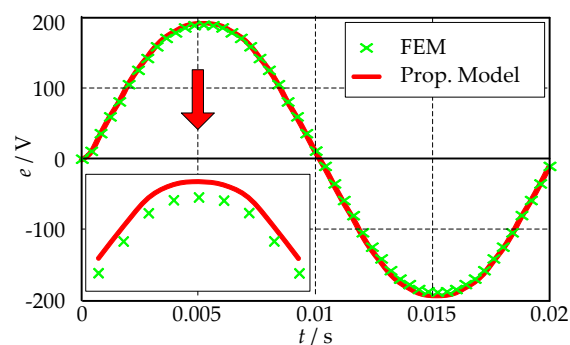


Figure 8. Phase electromotive force (EMF) of the proposed DRRF generator at no load.

The electromagnetic torque and its pulsating torques of the DRRF wind generator at full load are exhibited in Figure 9. The average value of the electromagnetic torque calculated by FEM is -39.6 Nm and that obtained by the analytical model is -39.7 Nm, which are very close to each other. As shown in Figure 9b, there are pulsating torques in the electromagnetic torque. One of them is the cogging torque, and the other is the ripple torque produced by the interaction of the harmonic components of the flux densities in both air gaps and the sinusoidal current in the DRRF generator. The torque ripple (the difference between maximum value and minimum value) of the electromagnetic torque is 3.69%.

When the inner and outer parts of the DRRF wind generator are designed with the same slot opening angle and pole arc ratio, the cogging torques produced by the inner and outer air gaps will be in phase, as shown in Figure 10, and the total cogging torque is their sum. According to Equation (60), the spatial period of the cogging torque is 2.5° . It can be seen that the cogging torque is satisfyingly low, since the wind turbine may never start with high cogging torque.

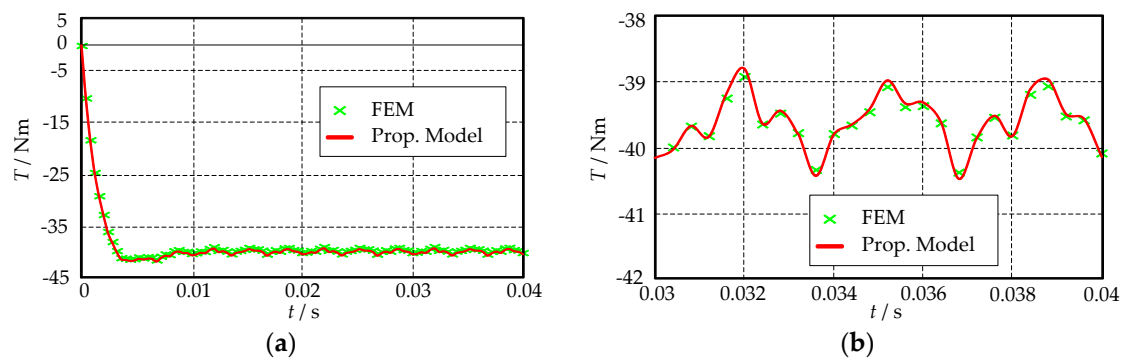


Figure 9. Electromagnetic torque and its pulsating torques of the proposed DRRF generator at full load: (a) Electromagnetic torque; (b) Pulsating torques in the electromagnetic torque.

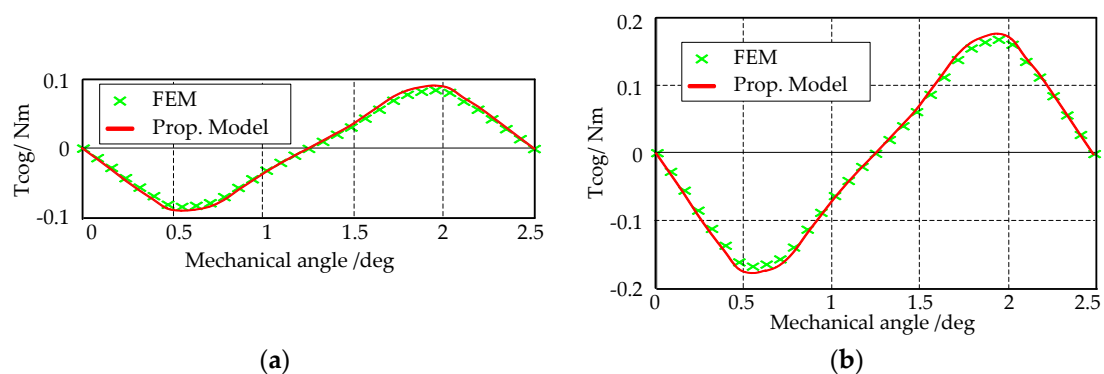


Figure 10. One cycle of cogging torque versus magnet rotor position of the DRRF wind generator: (a) Inner cogging torque; (b) Outer cogging torque.

Since the ferrite magnet is vulnerable to demagnetization, this risk is estimated by calculating the flux density of ferrite magnets. To analyze the irreversible demagnetization characteristics, five different measuring points in the inner and outer magnets are chosen respectively as shown in Figure 11. The flux densities of these points under no load operation at $-20\text{ }^{\circ}\text{C}$ in radial direction, which are the magnetization direction of the ferrite magnets, are shown in Figure 12. It can be seen that the flux density of point C_1 is closer to the demagnetization limit value than other points. This means that point C_1 is easier to be demagnetized. So point C_1 is selected to confirm the working points at different temperatures, and the working points are shown in Figure 13. The FEM results demonstrate that the DRRF wind generator is safe at all temperatures even at $-20\text{ }^{\circ}\text{C}$.

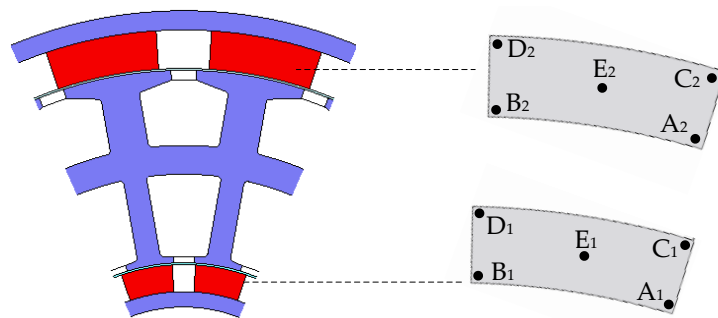


Figure 11. Different measuring points for analyzing the irreversible demagnetization characteristics.

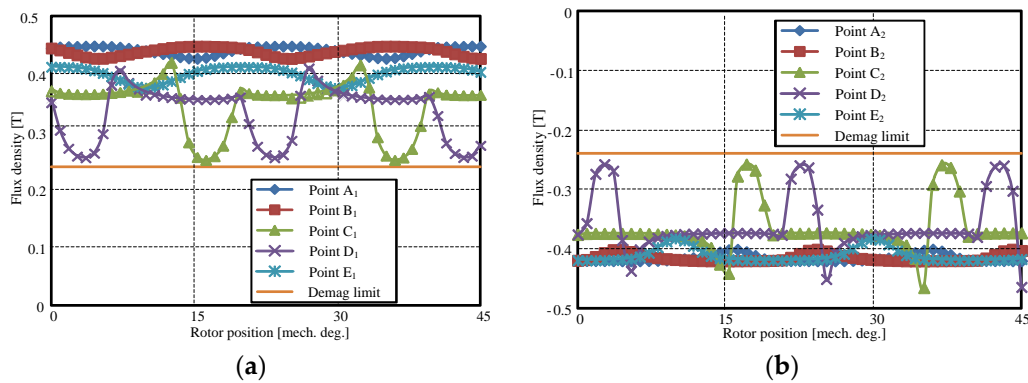


Figure 12. Flux densities (radial direction) of different locations of the magnets: (a) Points of the inner magnet; (b) Points of the outer magnet.

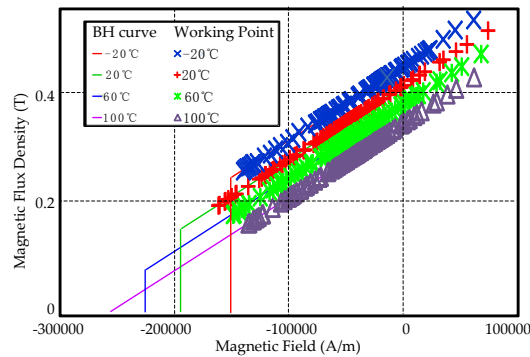


Figure 13. The working points of measuring point C₁.

4. Optimization by Finite Element Method (FEM)

A set of equations describing the generator performance are derived in Section 2 and their validity are proven by FEM in Section 3. However, designing a satisfying DRRF wind generator still needs optimization of some design parameters.

Due to the adoption of back-to-back toroidally wound winding, in order to take full advantage of the inner space, the area of the inner slot should equal to that of the outer slot. According to (46), we define the split ratio as $\lambda = R_{is}/R_{os}$, and then:

$$E_f = 4.44\sqrt{2}K_w f N_{ph} (B_{lg1}\lambda + B_{lg2}) R_{os} L / p \quad (61)$$

How λ affects E_f is shown in Figure 14, where it can be found that when λ is 0.43, E_f reaches the maximum value. The reason is given as follows: on the one hand, the smaller λ is, the larger the whole area of the inner and outer slots is, so there are more conductors for producing induced voltage. On the other hand, the smaller λ is, the smaller R_{is} is, and consequently there is less amount of magnet for producing induced voltage.

Torque ripple can generate acoustic noise, vibrations and mechanical stress in the wind turbine, thus, its minimization is highly required for wind power generations. Furthermore, the cogging torque caused by the tooth-slot structures, as an important component of the pulsating torque, must be minimized to better start wind power generator. There are several solutions to reduce the cogging torque, such as shifting the slot opening, shaping the magnets, skewing the stator or the magnets, varying slot opening angular width, and varying the pole arc ratio etc. By way of reducing manufacture cost, pole arc ratio design and shifting the slot opening are adopted to reduce the cogging torque.

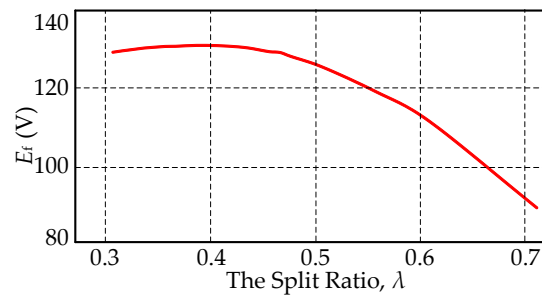


Figure 14. The back EMF is a function of the split ratio λ .

Since the energy stored in the outer air gap is more than that in the inner air gap, the total cogging torque of the DRRF generator is dominated by the outer portion. Therefore, the outer pole arc ratio α_{p2} is firstly optimized and then the inner ratio α_{p1} is secondly optimized. In fact, the pole arc ratio affects not only the cogging torque but also the THD of EMF. For the DRRF generator, how different α_{p1} and α_{p2} affect the cogging torque (peak-to-peak value, pk2pk) and THD of EMF is shown in Figure 15. To obtain a sinusoidal-induced voltage with low cogging torque, compromise selection of parameters is considered. With this consideration, the optimal value of α_{p2} is 0.67, and α_{p1} is 0.69.

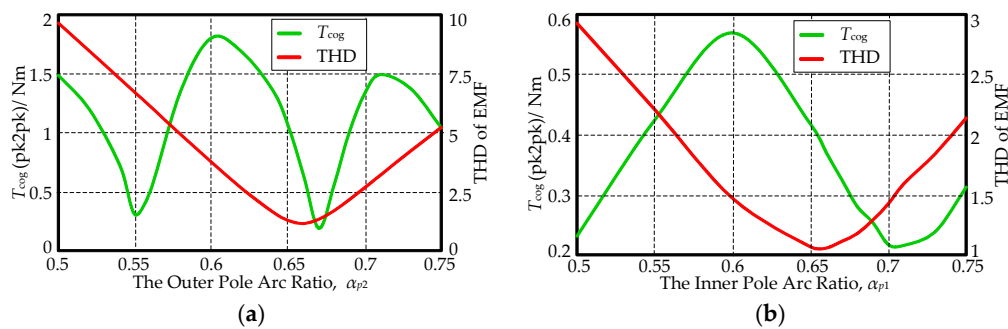


Figure 15. Cogging torque and THD as a function of the pole arc ratio: (a) The influence of outer pole arc ratio α_{p2} ; (b) The influence of inner pole arc ratio α_{p1} .

The cogging torque waveforms related to different pole arc ratios are demonstrated in Figure 16. It is shown that the maximum value of cogging torque is significantly reduced by optimizing the outer pole arc ratio α_{p2} . The inner pole arc ratio α_{p1} is also very important in this optimization. In this example, when $\alpha_{p2} = 0.67$ and $\alpha_{p1} = 0.65$, the maximum value of cogging torque reduces to 40% compared to that with $\alpha_{p2} = 0.67$ and $\alpha_{p1} = 0.69$.

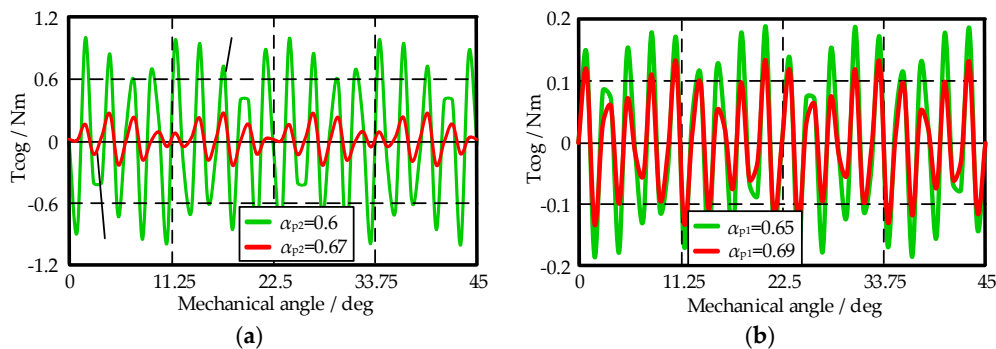


Figure 16. Comparison of cogging torques for the different pole arc ratio: (a) The influence of outer pole arc ratio α_{p2} ; (b) The influence of inner pole arc ratio α_{p1} .

For the slotted structure, the cogging torque decreases as the slot opening angular width decreases. For the same slot opening angular, the arc length of the outer slot opening is larger than that of the inner one. In order to reduce the cogging torque, the outer slot opening angular α_{bo2} can be designed to be smaller than α_{bo1} , as shown in Figure 17a. Figure 17b compares the cogging torque at different α_{bo2} . It can be seen that there is a big decline in the maximum cogging torque by changing α_{bo2} from 2.3° to 1.9° . This implies that changing the opening angular is a valid approach to reduce the cogging torque of the DRRF generator. But it should be known that this method cannot completely eliminate the cogging torque.

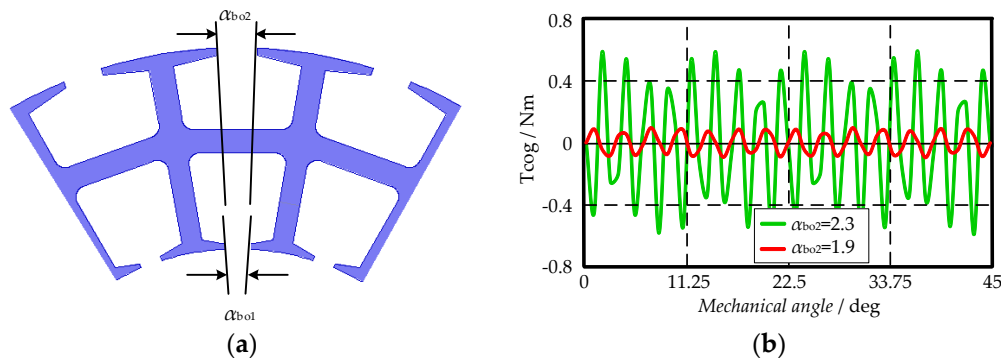


Figure 17. (a) Different slot opening angular $\alpha_{bo2} < \alpha_{bo1}$; (b) Comparison of cogging torques for different slot opening angular α_{bo2} .

5. Conclusions

In this paper, a comprehensive analytical model for a DRRF wind generator is developed based on EMC. Accurate calculations were performed, and results with rather high accuracy are obtained. The analytical model can precisely estimate the flux density distribution in the inner and outer air gaps as well as rotor and stator cores, back EMF waveform, both average and ripples of electro-magnetic torque, cogging torque, and other parameters. The results provided by the proposed model match well those from FEM analysis. That is, the analytical model developed in this paper can be employed in the preliminary design and analysis of the generator throughout the whole design process. Moreover, the working points of the ferrite magnets exceed the knee of the BH curve at different temperatures, which means the irreversible demagnetization does not occur at full load. Finally, the optimization is carried out by FEM to make the best use of the inner space of the generator, reduce the cogging torque, and decrease the THD of EMF. Accordingly, the optimal split ratio, pole arc ratio of the inner and outer rotor, as well as the outer slot opening has been obtained.

Acknowledgments: This work was supported in part by the National Natural Science Foundation of China under grant 51407085, the Postdoctoral Science Foundation of China under Award No. 2015M571685, the grant from the Priority Academic Program Development of Jiangsu Higher Education Institution and Jiangsu University Senior Talents Special Project under award 13JDG111.

Author Contributions: All authors contributed to this work by collaboration. Peifeng Xu, Kai Shi, Yuxin Sun and Huangqiu Zhu are the main authors of this manuscript.

Conflicts of Interest: The authors declare no conflict of interest.

References

1. Jia, S.F.; Qu, R.H.; Li, J.; Fan, X.G.; Zhang, M. Study of direct-drive permanent-magnet synchronous generators with solid rotor back iron and different windings. *IEEE Trans. Ind. Appl.* **2016**, *52*, 1369–1379.
2. Potgieter, J.H.J.; Kamper, M.J. Modeling and stability analysis of a direct-drive direct-grid slip-synchronous permanent-magnet Wind Generator. *IEEE Trans. Ind. Appl.* **2014**, *50*, 1738–1747. [[CrossRef](#)]

3. Chen, H.; Qu, R.H.; Li, J.; Li, D.W. Demagnetization performance of a 7 MW interior permanent magnet wind generator with fractional-slot concentrated windings. *IEEE Trans. Magn.* **2015**, *51*. [[CrossRef](#)]
4. Zhang, Z.Q.; Maveev, A.; Nilssen, R.; Nysveen, A. Ironless permanent-magnet generators for offshore wind turbines. *IEEE Trans. Ind. Appl.* **2014**, *50*, 1835–1846. [[CrossRef](#)]
5. Wang, D.; Liu, C.R.; Li, G.Y. An optimal integrated control scheme for permanent magnet synchronous generator-based wind turbine under asymmetrical grid fault conditions. *Energies* **2016**, *9*, 307. [[CrossRef](#)]
6. Kudrjavnsev, O.; Kilk, A.; Vaimann, T.; Belahcen, A.; Kallaste, A. Implementation of Different Magnetic Materials in Outer Rotor PM generator. In Proceedings of the 2015 IEEE 5th International Conference on Power Engineering, Energy and Electrical Drives (POWERENG), Riga, Latvia, 11–13 May 2015; pp. 74–78.
7. Boldea, I.; Tutulea, L.; Blaabjerg, F. High Power Wind Generator Designs with Less or No PMs: An Overview. In Proceedings of the 2014 17th International Conference on Electrical Machines and Systems (ICEMS), Hangzhou, China, 22–25 October 2014; pp. 1–14.
8. Vagati, A.; Boazzo, B.; Guglielmi, P.; Pellegrino, G. Design of ferrite-assisted synchronous reluctance machines robust toward demagnetization. *IEEE Trans. Ind. Appl.* **2014**, *50*, 1768–1779. [[CrossRef](#)]
9. Sergeant, P.; Van den Bossche, A.P.M. Influence of the amount of permanent-magnet material in fractional-slot permanent-magnet synchronous machines. *IEEE Trans. Ind. Electron.* **2014**, *61*, 4979–4989. [[CrossRef](#)]
10. Nakamura, K.; Ichinokura, O. Super-multipolar permanent magnet reluctance generator designed for small-scale wind turbine generation. *IEEE Trans. Magn.* **2012**, *48*, 3311–3314. [[CrossRef](#)]
11. Jang, S.M.; Seo, H.J.; Park, Y.S.; Park, H.I.; Choi, J.Y. Design and electromagnetic field characteristic analysis of 1.5 kW small scale wind power generator for substitution of Nd-Fe-B to ferrite permanent magnet. *IEEE Trans. Magn.* **2012**, *48*, 2933–2936. [[CrossRef](#)]
12. Qu, R.H.; Lipo, T.A. Dual-Rotor, Radial-Flux, Toroidally-Wound, Permanent-Magnet Machines. In Proceedings of the 2002 Industry Applications Conference, 37th IAS Annual Meeting, Lubbock, TX, USA, 13–18 October 2002; pp. 1281–1288.
13. Wang, J.; Qu, R.H.; Zhou, L.B. Dual-Rotor multiphase permanent magnet machine with harmonic injection to enhance torque density. *IEEE Trans. Appl. Supercond.* **2012**, *22*. [[CrossRef](#)]
14. Zhao, W.L.; Lipo, T.A.; Kwon, B.I. A novel dual-rotor, axial field, fault-tolerant flux-switching permanent magnet machine with high-torque performance. *IEEE Trans. Magn.* **2015**, *51*. [[CrossRef](#)]
15. Qu, R.H.; Lipo, T.A. Design and parameter effect analysis of dual-rotor, radial-flux, toroidally wound, permanent-magnet machines. *IEEE Trans. Ind. Appl.* **2004**, *40*, 771–779. [[CrossRef](#)]
16. Qu, R.H.; Lipo, T.A. Dual-rotor, radial-flux, toroidally wound, permanent-magnet machines. *IEEE Trans. Ind. Appl.* **2003**, *39*, 1665–1673.
17. Lim, D.K.; Woo, D.K.; Kim, I.W.; Ro, J.S.; Jung, H.K. Cogging torque minimization of a dual-type axial-flux permanent magnet using a novel optimal algorithm. *IEEE Trans. Magn.* **2013**, *49*, 5106–5111. [[CrossRef](#)]
18. Qu, R.H.; Aydin, M.; Lipo, T.A. Performance Comparison of Dual-Rotor Radial-Flux and Axial-Flux Permanent-Magnet BLDC Machine. In Proceedings of the 2003 IEEE International Electric Machines and Drives Conference (IEMDC), Madison, WI, USA, 1–4 June 2003; pp. 1948–1954.
19. Mohammadi, S.; Mirsalim, M. Double-sided permanent-magnet radial-flux eddy-current couplers: Three-dimensional analytical modeling, static and transient study, and sensitivity analysis. *IET Electr. Power Appl.* **2013**, *7*, 665–679. [[CrossRef](#)]
20. Azizi, D.; Gholami, A. Multiobjective optimization of stator slot insulation of high-voltage generator based on coupled SNOPT-finite element method analysis. *IEEE Electr. Insul. Mag.* **2013**, *29*, 69–76. [[CrossRef](#)]
21. Lipo, T.A. *Introduction to AC Machine Design*, 1st ed.; Wisconsin Power Electronics Research Center, University of Wisconsin-Madison: Madison, WI, USA, 1998; pp. 24–99.

